

# EFFECT OF MASK REGIONS ON WEAK LENSING STATISTICS

MASATO SHIRASAKI

Department of Physics, University of Tokyo, Tokyo 113-0033, Japan

NAOKI YOSHIDA

Department of Physics, University of Tokyo, Tokyo 113-0033, Japan

Kavli Institute for the Physics and Mathematics of the Universe (WPI), University of Tokyo, Kashiwa, Chiba 277-8583, Japan

AND

TAKASHI HAMANA

National Astronomical Observatory of Japan, Tokyo 181-0015, Japan

*Draft version July 7, 2018*

## ABSTRACT

Sky masking is unavoidable in wide-field weak lensing observations. We study how masks affect the measurement of statistics of matter distribution probed by weak gravitational lensing. We first use 1000 cosmological ray-tracing simulations to examine in detail the impact of masked regions on the weak lensing Minkowski Functionals (MFs). We consider actual sky masks used for a Subaru Suprime-Cam imaging survey. The masks increase the variance of the convergence field and the expected values of the MFs are biased. The bias then affects the non-Gaussian signals induced by the gravitational growth of structure. We then explore how masks affect cosmological parameter estimation. We calculate the cumulative signal-to-noise ratio S/N for masked maps to study the information content of lensing MFs. We show that the degradation of S/N for masked maps is mainly determined by the effective survey area. We also perform simple  $\chi^2$  analysis to show the impact of lensing MF bias due to masked regions. Finally, we compare ray-tracing simulations with data from a Subaru 2 deg<sup>2</sup> survey in order to address if the observed lensing MFs are consistent with those of the standard cosmology. The resulting  $\chi^2/n_{\text{dof}} = 29.6/30$  for three combined MFs, obtained with the mask effects taken into account, suggests that the observational data are indeed consistent with the standard  $\Lambda$ CDM model. We conclude that the lensing MFs are powerful probe of cosmology only if mask effects are correctly taken into account.

## 1. INTRODUCTION

An array of recent observations such as the cosmic microwave background (CMB) anisotropies (e.g. Komatsu et al. 2011; Planck Collaboration et al. 2013) and the large-scale structure (e.g. Tegmark et al. 2006; Reid et al. 2010) established the standard  $\Lambda$ CDM model. The energy content of the present-day universe is dominated by dark energy and dark matter, and the primordial density fluctuations, which seeded all rich structure that we observe today, were generated through inflation in the very early universe. A few important questions still remain such as the nature of dark energy, the physical properties of dark matter, and the exact mechanism that generates the primordial density fluctuations.

Gravitational lensing is a powerful method to study matter distribution (e.g. Oguri et al. 2012). Future weak lensing surveys are aimed at measuring cosmic shear over a wide area of more than a thousand square degrees. Such observational programmes include the Subaru Hyper Suprime-Cam (HSC)<sup>1</sup>, the Dark Energy Survey (DES)<sup>2</sup>, and the Large Synoptic Survey Telescope (LSST)<sup>3</sup>. Space missions such as Euclid and WFIRST are also promising. The large set of cosmic shear data

will enable us to improve the constraints on cosmological parameters which will provide important clues to the mysterious dark components.

A variety of statistics are proposed to characterize the large-scale matter distribution. Minkowski Functionals (MFs) are among the most useful statistics to extract non-Gaussian information from a two-dimensional or three-dimensional field. For example, MFs have been applied to the observed CMB maps and provided comparable constraints to those obtained using the CMB bispectrum (Hikage et al. 2008). Matsubara & Jain (2001) and Sato et al. (2001) studied  $\Omega_m$ -dependence of weak lensing MFs. More recently, Kratochvil et al. (2012) showed that the lensing MFs contain significant cosmological information, beyond the power-spectrum, whereas Shirasaki et al. (2012) showed that weak lensing MFs can be used to constrain the statistical properties of the primordial density fluctuations.

These previous studies on weak lensing MFs often consider idealized cases. However, many observational effects are present in real weak lensing measurements, for example, imperfect shape measurement due to seeing and optical distortion, selection effects of galaxies, uncertain redshift distribution of galaxies due to photometric redshift error (e.g. Bolzonella et al. 2000), noise-rectification biases (e.g. Kaiser 2000; Erben et al. 2001; Hirata & Seljak 2003), and complicated survey geometry due to masked regions. Some of these effects on cosmic

masato.shirasaki@utap.phys.s.u-tokyo.ac.jp

<sup>1</sup> [http://www.naoj.org/Projects/HSC/j\\_index.html](http://www.naoj.org/Projects/HSC/j_index.html)

<sup>2</sup> <http://www.darkenergysurvey.org/>

<sup>3</sup> <http://www.lsst.org/lsst/>

shear power spectrum analysis have been already studied (e.g. Huterer et al. 2006; Hikage et al. 2011). A comprehensive study of observational effects on lensing MFs is also needed in order to fully exploit the data from upcoming wide cosmology surveys.

In the present paper, we study the impact of masked regions on the measurement of weak lensing MFs. Masking effect could be one of the major systematics because MFs are intrinsically morphological quantities. We use a large set of numerical simulations to critically examine the effect of masking. We then directly measure the lensing MFs from real observational data obtained from a Subaru survey. We compare the observed MFs with the results of our ray-tracing simulations that explicitly include the effect of masked regions.

The rest of the present paper is organized as follows. In Section 2, we summarize the basics of MFs and how to estimate MFs from observed shear field. In Section 3, we describe the data used in this paper and the details of numerical simulations of gravitational lensing. In Section 4, we show the results of the impact of masked regions on lensing MFs. We also perform a simple analysis to characterize the impact of masked regions on cosmological constraints from lensing MFs. We then represent the comparison with observed MFs and ray-tracing simulation results. Concluding remarks and discussions are given in Section 5.

## 2. MINKOWSKI FUNCTIONALS

### 2.1. Basics

MFs are morphological statistics for some smoothed random field above a certain threshold. In general, for a given  $D$ -dimensional smoothed field  $\mathbb{S}^D$ , one can calculate  $D+1$  MFs  $V_i$ . On  $\mathbb{S}^2$ , one can thus define 2+1 MFs  $V_0, V_1$ , and  $V_2$ . For a given threshold,  $V_0$ ,  $V_1$ , and  $V_2$  describe the fraction of area, the total boundary length of contours, and the integral of the geodesic curvature  $K$  along the contours, respectively. MFs are defined, for threshold  $\nu$ , as

$$V_0(\nu) \equiv \frac{1}{4\pi} \int_{Q_\nu} dS, \quad (1)$$

$$V_1(\nu) \equiv \frac{1}{4\pi} \int_{\partial Q_\nu} \frac{1}{4} d\ell, \quad (2)$$

$$V_2(\nu) \equiv \frac{1}{4\pi} \int_{\partial Q_\nu} \frac{1}{2\pi} K d\ell, \quad (3)$$

where  $Q_\nu$  and  $\partial Q_\nu$  represent the excursion set and the boundary of the excursion set for a smoothed field  $u(\boldsymbol{\theta})$ . They are given by

$$Q_\nu = \{\boldsymbol{\theta} | u(\boldsymbol{\theta}) > \nu\}, \quad (4)$$

$$\partial Q_\nu = \{\boldsymbol{\theta} | u(\boldsymbol{\theta}) = \nu\}. \quad (5)$$

For a two-dimensional Gaussian random field, one can calculate the expectation values for MFs analytically (Tomita 1986):

$$V_0(\nu) = \frac{1}{2} \left[ 1 - \text{erf} \left( \frac{\nu - \mu}{\sigma_0} \right) \right], \quad (6)$$

$$V_1(\nu) = \frac{1}{8\sqrt{2}} \frac{\sigma_1}{\sigma_0} \exp \left( -\frac{(\nu - \mu)^2}{\sigma_0^2} \right), \quad (7)$$

$$V_2(\nu) = \frac{\nu - \mu}{2(2\pi)^{3/2}} \frac{\sigma_1^2}{\sigma_0^3} \exp \left( -\frac{(\nu - \mu)^2}{\sigma_0^2} \right), \quad (8)$$

where  $\mu = \langle u \rangle$ ,  $\sigma_0^2 = \langle u^2 \rangle - \mu^2$ , and  $\sigma_1^2 = \langle |\nabla u|^2 \rangle$ .

### 2.2. Estimation of Lensing MFs from Cosmic Shear Data

We summarize how to estimate lensing MFs from observed shear data. Let us first define the weak lensing mass maps that correspond to the smoothed lensing convergence field  $\kappa$ :

$$\mathcal{K}(\boldsymbol{\theta}) = \int d^2\phi \kappa(\boldsymbol{\theta} - \boldsymbol{\phi}) U(\boldsymbol{\phi}), \quad (9)$$

where  $U$  is the filter function to be specified below. We can calculate the same quantity by smoothing the shear field  $\gamma$  as

$$\mathcal{K}(\boldsymbol{\theta}) = \int d^2\phi \gamma_t(\boldsymbol{\phi} : \boldsymbol{\theta}) Q_t(\boldsymbol{\phi}), \quad (10)$$

where  $\gamma_t$  is the tangential component of the shear at position  $\boldsymbol{\phi}$  relative to point  $\boldsymbol{\theta}$ . The filter function for the shear field  $Q_t$  relates to  $U$  by

$$Q_t(\boldsymbol{\theta}) = \int_0^{\theta_o} d\theta' \theta' U(\theta') - U(\theta). \quad (11)$$

We consider  $Q_t$  to be defined with a finite extent. In this case, one finds

$$U(\theta) = 2 \int_\theta^{\theta_o} d\theta' \frac{Q_t(\theta')}{\theta'} - Q_t(\theta), \quad (12)$$

where  $\theta_o$  is the outer boundary of the filter function.

In the following, we consider the truncated Gaussian filter (for  $U$ ) as

$$U(\theta) = \frac{1}{\pi\theta_G^2} \exp \left( -\frac{\theta^2}{\theta_G^2} \right) - \frac{1}{\pi\theta_o^2} \left( 1 - \exp \left( -\frac{\theta_o^2}{\theta_G^2} \right) \right), \quad (13)$$

$$Q_t(\theta) = \frac{1}{\pi\theta^2} \left[ 1 - \left( 1 + \frac{\theta^2}{\theta_G^2} \right) \exp \left( -\frac{\theta^2}{\theta_G^2} \right) \right], \quad (14)$$

for  $\theta \leq \theta_o$  and  $U = Q_t = 0$  elsewhere. Throughout the present paper, we adopt  $\theta_G = 1'$  and  $\theta_o = 15'$ . Note that this choice of  $\theta_G$  corresponds to an optimal smoothing scale for the detection of massive galaxy clusters using weak lensing with  $z_{\text{source}} = 1.0$  (Hamana et al. 2004).

We follow Lim & Simon (2012) in calculating the MFs from pixelated  $\mathcal{K}$  maps. We convert a weak lensing field  $\mathcal{K}$  to  $x = (\mathcal{K} - \langle \mathcal{K} \rangle) / \sigma_0$  where  $\sigma_0$  is the standard deviation of  $\mathcal{K}$ . In binning the thresholds, we set  $\Delta x = 0.2$  from  $x = -5$  to  $x = 5$ . It is possible that the above normalization affects the MFs through the variance of  $\sigma_0$  for each field. In light of this, Weinberg et al. (1987) suggest an alternative definition that a density contour with a certain threshold  $\nu_V$  is related to the fraction of volume  $f$  where

$$f = (2\pi)^{-1/2} \int_{\nu_V}^{\infty} e^{-t^2/2} dt. \quad (15)$$

Using  $\nu_V$  instead of  $x$  apparently avoids the normalization issue for MFs at least technically. However, even with  $\nu_V$ , we cannot eliminate the effect of the variance

between multiple fields because the  $f - \nu_V$  mapping needs to be done for each field or for each sample, rather than by using some global quantity calculated for all the samples. We have explicitly tested the effect of the sample variance of  $\sigma_0$  on MFs against  $\nu_V$  and  $x$  using 1000 Gaussian simulations<sup>1</sup>.

In Figure 1, we compare the mean of  $V_2$  MFs over our 1000 Gaussian maps with the Gaussian prediction given by Eq. (8). For the Gaussian prediction, we calculate the quantities  $\langle \mathcal{K} \rangle$ ,  $\sigma_0$  and  $\sigma_1$  by averaging over 1000 realizations; these quantities serve as ‘global’ values. The error bars in each plot represent the variance of  $V_2$  around the global mean. The three panels differ in that the MFs are plotted as a function of, from left to right,  $\mathcal{K} - \langle \mathcal{K} \rangle$ ,  $(\mathcal{K} - \langle \mathcal{K} \rangle)/\sigma_0$ , and  $\nu_V$ , respectively. The apparent variation of the MFs, namely error bars, in the middle and right panels is partly caused by the variance of the measured  $\sigma_0$  for each field. In the lower panels, we show the difference between the mean  $V_2$  and the Gaussian prediction. The difference should be compared with the field variance that is indicated by error bars. Note that the difference from the Gaussian prediction is larger than the field variance when the MFs are evaluated with normalization as  $(\mathcal{K} - \langle \mathcal{K} \rangle)/\sigma_0$  or by using  $\nu_V$  associated with volume fraction (Eq. (15)). As expected, the Gaussian prediction describes the mean MFs well as long as the MFs are evaluated *without* normalization of  $\mathcal{K}$  by  $\sigma_0$  (left panel). However, we cannot use weak lensing field  $\mathcal{K}$  directly when we compare theoretical predictions with the observation of a limited area (with masks). Theoretical predictions for MFs are always given as a function of some normalized threshold. One thus needs either to de-normalize the theoretical prediction by using an appropriate variance for the observed field, or to normalize the observed  $\mathcal{K}$  in some way. In other words, field-to-field variance of the weak lensing MFs is caused partly by the variance  $\sigma_0$ , and thus statistical analysis such as cosmological parameter estimation should be done by including the field variance of  $\sigma_0$ . In the rest of this paper, we simply use the normalized field  $x = (\mathcal{K} - \langle \mathcal{K} \rangle)/\sigma_0$  for estimation of MFs. When we estimate lensing MFs on a  $\mathcal{K}$  map with mask, we discard the pixels within  $2\theta_G$  from the mask boundaries, because  $\mathcal{K}$  data on such regions are affected by the lack of shear data.

### 3. DATA

#### 3.1. *Suprime-Cam*

We use the  $i'$ -band data from the Subaru/Suprime-Cam data archive **SMOKA**<sup>1</sup>. The observation is characterized as follows. The area is contiguous with at least four pointings, the exposure time for each pointing is longer than 1800 sec, and the seeing full width at half-maximum (FWHM) is better than 0.65 arcsec. The data are dubbed “COSMOS” in Table A1 in Hamana et al. (2012).

<sup>1</sup> We generate the Gaussian convergence maps for LCDM cosmology using the fitting formula of Smith et al. (2003) to calculate the matter power spectrum  $P(k; z)$ . We then integrate the matter power spectrum over redshift  $z$ , convolved with a weighting function for the source redshift  $z_{\text{source}} = 1$ . Each convergence map is defined on  $2048^2$  grid points with an angular grid size of 0.15 arcmin.

<sup>1</sup> <http://smoka.nao.ac.jp/>

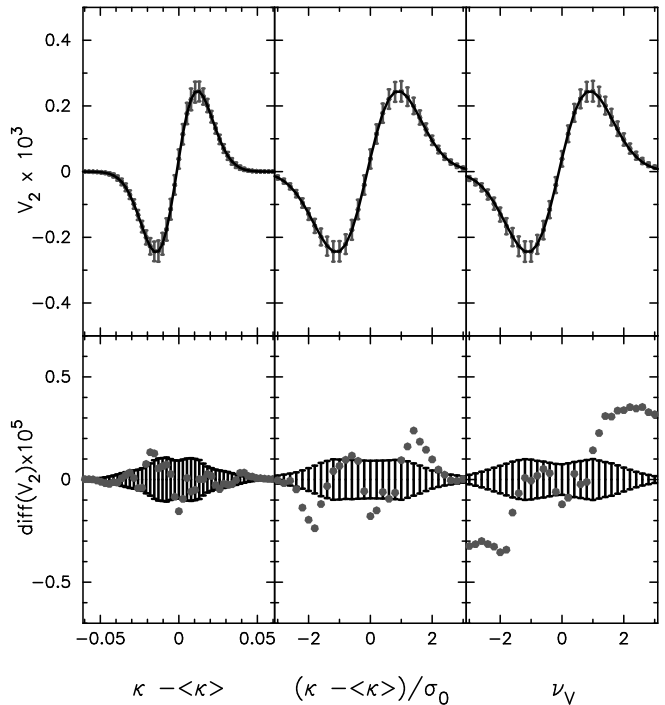


FIG. 1.— The effect of sample variance of field variance  $\sigma_0$  on MFs. We compare the mean  $V_2$  over 1000 maps with the Gaussian prediction of Eq. (8).  $V_2$  in the left panel is calculated without normalization whereas that in the middle panel is calculated for each  $\mathcal{K}$  field normalized by its variance and that in the right panel is calculated for each  $\nu_V$  (see text and the horizontal axes label). The gray points in the lower portion show the differences between the mean  $V_2$  and the Gaussian prediction. The differences are also compared with the variance of  $V_2$  estimated from our 1000 gaussian maps (black error bars), i.e. the standard deviation of  $V_2$  divided by  $\sqrt{1000}$ .

We conservatively use the data only within a 15 arcmin radius from the field center of Suprime-Cam, because the point spread function (PSF) becomes elongated significantly outside of the central area, which may make PSF correction inaccurate. Then mosaic stacking is performed with **SCAMP** (Bertin 2006) and **SWarp** (Bertin et al. 2002). We use **SExtractor** (Bertin & Arnouts 1996) and **hfindpeaks** of the software **IMCAT** software (Kaiser et al. 1995), and then the two catalogs are merged by matching positions of the detected objects with a tolerance of 1 arcsec.

For weak lensing analysis, we follow the KSB method (Kaiser et al. 1995; Luppino & Kaiser 1997; Hoekstra et al. 1998). Stars are selected in the standard way by identifying the appropriate branch in the magnitude half-light radius ( $rh$ ) plane, along with the detection significance cut  $S/N > 10$ . We found that the number density of stars is  $\sim 1 \text{ arcmin}^{-2}$ . We use the galaxy images that satisfy the following three conditions; (i) the detection significance of  $S/N > 3$  and  $\nu > 10$  where  $\nu$  is an estimate of the peak significance given by **hfindpeaks**, (ii)  $rh$  is larger than the stellar branch, and (iii) the AB magnitude is in the range of  $22 < i' < 25$  (where **MAG\_AUTO** given by **SExtractor** is used for the magnitude and slightly different from Hamana et al. (2012)). The resulting number density of galaxies  $n_{\text{gal}}$  is then  $15.8 \text{ arcmin}^{-2}$ . We measure the shapes of the objects using **getshapes** in **IMCAT**, and correct for the PSF

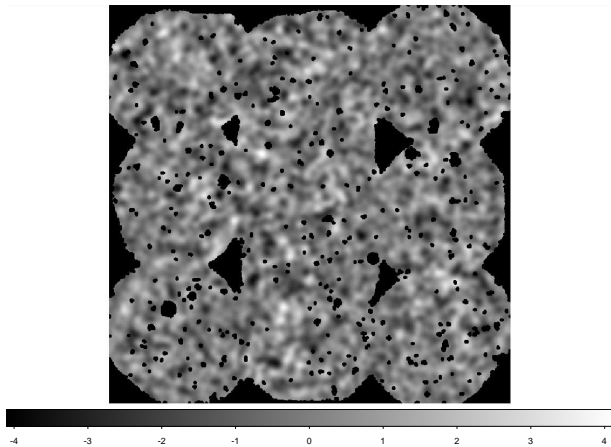


FIG. 2.— The reconstructed lensing field  $\mathcal{K}$  from the Subaru Suprime-Cam data. The convergence  $\mathcal{K}$  is computed from the ellipticity of 102342 source galaxies by Eq.(10). The masked survey area (black portion) covers  $0.34 \text{ deg}^2$ . The grey-scale bar shows the value of  $(\mathcal{K} - \langle \mathcal{K} \rangle)/\sigma_0$ .

using the KSB method. The *rms* of the galaxy ellipticities after the PSF correction is 0.314.

Next, we define data and masked regions by using the observed positions of the source galaxies as follows. We map the observation area onto rectangular pixels of width 0.15 arcmin. For each pixel, we check if there is a galaxy within  $\theta_D = 0.4$  arcmin from the pixel center. If there are no galaxies, then the pixel is marked as a mask pixel. After performing the procedure for all the pixels, the marked pixels are masked regions, whereas the other pixels are data regions. However, we unmask “isolated” masked pixels whose surrounding pixels are all data pixels.

Weak lensing convergence field  $\mathcal{K}$  is computed from the galaxy ellipticity data as in Eq. (10) on regular grids with a grid spacing of 0.15 arcmin. The resulting mass map includes masked regions as shown in Figure 2. The masked regions cover  $0.34 \text{ deg}^2$  in total. The unmasked regions are found to be  $1.79 \text{ deg}^2$ . Note that we use only  $0.575 \text{ deg}^2$  in unmasked regions for lensing MFs analysis because we remove the ill-defined pixels within  $2\theta_G = 2$  arcmin from the boundary of the mask.

### 3.2. Ray-tracing Simulation

In order to study the impact of masked regions on lensing MFs, we use 1000 weak gravitational lensing ray-tracing simulations from Sato et al. (2009)<sup>2</sup>. The ray-tracing simulations are performed on light-cone outputs that are generated by arranging multiple simulation boxes. Briefly, small- and large-volume  $N$ -body simulations are placed to cover a past light-cone of a hypothetical observer with an angular extent of  $5^\circ \times 5^\circ$ , from redshift  $z = 0$  to  $z = 3.5$ , similarly to the methods in White & Hu (2000) and Hamana & Mellier (2001). We set the source redshift  $z_{\text{source}} = 1$  for the ray-tracing simulations. Each map is defined on  $2048^2$  grid points with an angular grid size of 0.15 arcmin. Details of the ray-tracing simulations are found in Sato et al. (2009).

<sup>2</sup> For the simulations, the adopted cosmology is consistent with WMAP3 results (Spergel et al. 2007).

It is well-known that the intrinsic ellipticities of source galaxies induce noises to lensing shear maps. We model the noise by adding random ellipticities drawn from a two-dimensional Gaussian to the simulated shear data. We set the root-mean-square of intrinsic ellipticities to be 0.314 and the number of source galaxies is set  $15.8 \text{ arcmin}^{-2}$ . The values are obtained from the actual weak lensing observations described in Section 3.1.

## 4. RESULT

### 4.1. Masking Effect on Lensing MFs

We first discuss the overall effect of masking on the lensing MFs. To this end, we use ray-tracing simulations of weak gravitational lensing described in Section 3.2. We pay particular attention to non-Gaussian features in the case with masks. The total non-Gaussianity probed by the lensing MFs  $\Delta V_i^{\text{obs}}$  is given by

$$\Delta V_i^{\text{obs}} = V_i(\text{masked}) - V_i^G(\text{masked}), \quad (16)$$

where  $V_i(\text{masked})$  is  $i$ -th MF on a masked map and  $V_i^G(\text{masked})$  is the Gaussian term of  $V_i(\text{masked})$ .

We can then decompose  $\Delta V_i^{\text{obs}}$  into three components:

$$\Delta V_i^{\text{obs}} = \Delta V_i^{\text{gravity}} + \Delta V_i^{\text{bias}} - \Delta V_i^{\text{bias,G}}, \quad (17)$$

$$\Delta V_i^{\text{gravity}} = V_i(\text{unmasked}) - V_i^G(\text{unmasked}), \quad (18)$$

$$\Delta V_i^{\text{bias}} = V_i(\text{masked}) - V_i(\text{unmasked}), \quad (19)$$

$$\Delta V_i^{\text{bias,G}} = V_i^G(\text{masked}) - V_i^G(\text{unmasked}), \quad (20)$$

where  $\Delta V_i^{\text{gravity}}$  represents the non-Gaussianity induced by non linear gravitational growth,  $\Delta V_i^{\text{bias}}$  describes the mask bias of MFs for non-Gaussian maps, and  $\Delta V_i^{\text{bias,G}}$  corresponds to the Gaussian term of  $\Delta V_i^{\text{bias}}$ . In order to calculate these quantities, we first need to calculate  $V_i^G(\text{masked})$  and  $V_i^G(\text{unmasked})$ . For this purpose, we measure the following three quantities from 1000 masked ray-tracing maps:

$$\mu = \langle \mathcal{K} \rangle, \quad \sigma_0^2 = \langle \mathcal{K}^2 \rangle - \mu^2, \quad \sigma_1^2 = \langle |\nabla \mathcal{K}|^2 \rangle. \quad (21)$$

The same quantities are measured also for the unmasked lensing maps. We can then estimate  $V_i^G(\text{masked})$  and  $V_i^G(\text{unmasked})$  using these quantities and Eq. (6)-(8). For the Gaussian terms, we also consider the correction of the finite binning effect pointed out by Lim & Simon (2012). The correction is needed because the threshold  $\nu$  to calculate the MFs  $V_1$  and  $V_2$  is not continuous but discrete with some finite width. We calculate the correction by integrating the analytic formula (Eq. (7),(8)) for finite binning width (see Lim & Simon (2012) for details). We then estimate  $V_i(\text{masked})$  and  $V_i(\text{unmasked})$  directly from masked and unmasked maps. Figure 3 shows the various non-Gaussian contributions (Eq. (17)-(20)) calculated directly from 1000 masked ray-tracing maps. We find that  $\Delta V_i^{\text{bias}}$  is comparable to  $\Delta V_i^{\text{gravity}}$  in the ray-tracing maps. The mask bias  $\Delta V_i^{\text{bias}}$  contributes significantly to the observed non-Gaussianity  $\Delta V_i^{\text{obs}}$ . Note also that  $\Delta V_i^{\text{bias,G}}$  is sub-dominant although not negligible for  $V_1$  and  $V_2$ . Clearly the mask bias can be a significant contaminant for cosmological parameter estimation using

the lensing MFs. In the following, we include the bias effect when comparing simulation data and observations.

#### 4.2. Impact of Masking on Cosmological Parameter Estimation

We next study cosmological information content in the lensing MFs with masks. An important quantity is the cumulative signal-to-noise ratio  $S/N$  for lensing MFs, which is defined by

$$(S/N)^2 = \boldsymbol{\mu}^t \mathbf{C}^{-1} \boldsymbol{\mu}, \quad (22)$$

where  $\boldsymbol{\mu}$  is a data vector that consists of the lensing MFs  $V_0$ ,  $V_1$ , and  $V_2$ , and  $\mathbf{C}$  is the covariance matrix. In order to calculate  $(S/N)^2$ , we construct the data vector from a set of lensing MFs as

$$\{\mu_i\} = \{V_0(x_1), \dots, V_0(x_{10}), V_1(x_1), \dots, V_1(x_{10}), V_2(x_1), \dots, V_2(x_{10})\}, \quad (23)$$

where  $x_i = (\mathcal{K}_i - \langle \mathcal{K} \rangle) / \sigma_0$  is the binned normalized lensing field. We calculate the covariance matrix of MFs using 1000 ray-tracing simulations.

Figure 4 shows the cumulative signal-to-noise ratio  $S/N$  as a function of  $x_i$ . Clearly the information content is reduced by a factor of two in the case with mask. The degradation is explained by the reduced effective area. The solid line shows  $S/N$  by scaling  $\mathbf{C}^{-1}$  with the effective survey area. It closely matches the  $S/N$  calculated directly from the masked maps. For a Gaussian random field, we expect that the variance of MFs should be inversely proportional to the effective survey area (e.g. Winitzki & Kosowsky 1998; Wang et al. 2009). The result shown in Figure 4 suggests that the effective survey area mainly determines how much cosmological information we can gain from weak lensing MFs.

Let us further quantify the overall impact of bias of the lensing MFs. We perform the following simple analysis to investigate the effect of the mask bias on cosmological parameter estimation. For each realization  $r$  of our simulations, we calculate the  $\chi^2$  value as follows,

$$\chi^2(r) = (\mu_i(r) - \mu_i^{\text{theory}}) \mathbf{C}^{-1} (\mu_j(r) - \mu_j^{\text{theory}}), \quad (24)$$

where  $\mu_i(r)$  is the estimated lensing MFs from each realization  $r$  and  $\mu_i^{\text{theory}}$  is the theoretical template for a given cosmology. In practice, we assume that  $\mu_i^{\text{theory}}$  is the average over our 1000 ray-tracing simulations with or without masks. The lensing MFs  $\mu_i(r)$  are estimated for each masked map, and then we use the covariance matrices of the MFs obtained from a total of 1000 masked maps. If  $\mu_i(r)$  follows the Gaussian distribution, the distribution of  $\chi^2(r)$  should follow a genuine  $\chi^2$  distribution. We can then clearly see the impact of bias due to masking on cosmological constraints by comparing the resulting distribution of  $\chi^2(r)$  for  $\mu_i^{\text{theory}}$  estimated from unmasked maps.

Figure 5 shows the resulting distribution of  $\chi^2(r)$  for our 1000 masked ray-tracing simulations. The black histogram is the probability of  $\chi^2(r)$  for the corresponding model using the average MFs over the masked maps whereas the gray one is for the unmasked maps. The thick solid line is a genuine  $\chi^2$  distribution with 30 degrees of freedom, and the dashed line indicates the  $1\sigma$

region for the  $\chi^2$  values. We find an excellent agreement between the thin histogram and the solid line. This means that the binned lensing MFs  $\mu_i(r)$  can be described well by a Gaussian distribution. Interestingly, most of the resulting  $\chi^2(r)$  without mask lie outside  $1\sigma$  regions. When we do not take account of bias due to masked regions, 55.3%, 59.4%, 74.9% and 85.4% of the realizations lies outside  $1\sigma$  regions of the  $\chi^2$  values for  $V_0$ ,  $V_1$ ,  $V_2$  and all MFs. We conclude that the bias of lensing MFs due to masked regions can crucially affect a cosmological parameter estimation.

#### 4.3. Application to Subaru Suprime-Cam Data

It is important to test whether we can extract cosmological information from masked noisy shear data using the lensing MFs. To this end, we use available Subaru Suprime-Cam data. We analyze the observed weak lensing map by using the statistics derived from a large set of ray-tracing simulations. We include observational effects directly in our simulations, i.e., masked regions and shape noises as described in Section 3.2. Figure 6 compares the lensing MFs for the Subaru data and those calculated for the ray-tracing simulations. We plot the MFs  $V_0$ ,  $V_1$ , and  $V_2$  in the top panels. In the bottom panels, the thick error bars show the cosmic variance of lensing MFs estimated from our 1000 simulated maps, whereas the thin error bars are the sum of the cosmic variance and the statistical error. We estimate the statistical error from 1000 randomized realizations, in which the ellipticity of each source galaxy is rotated randomly. The statistical error is approximately  $\sim 1.5$  times the cosmic variance for each bin. In order to quantify the consistency of our results, we perform a so-called  $\chi^2$  analysis. We compute the  $\chi^2$  statistics for the observed lensing MFs,

$$\chi^2 = (d_i - m_i) \mathbf{C}_{\text{cv+stat}}^{-1} (d_j - m_j) \quad (25)$$

where  $d_i$  is the lensing MFs in the  $i$ -th bin for observation,  $m_i$  is the theoretical model, and  $\mathbf{C}_{\text{cv+stat}}$  is the covariance matrix of lensing MFs including the cosmic variance and the statistical error. The cosmic variances are estimated from 1000 ray-tracing simulations, and the statistical errors are computed from 1000 randomized galaxy catalogs. We estimate  $m_i$  by averaging the MFs over 1000 ray-tracing simulations. We use 10 bins in the range of  $x = [-3, 3]$  for each MF. For the binning, we have a sufficient number of simulations to estimate the covariance matrix of the lensing MFs. The resulting value of  $\chi^2$  per number of freedoms is  $\chi^2/n_{\text{dof}} = 3.35/10, 9.69/10, 12.8/10$  and  $29.6/30$  for  $V_0$ ,  $V_1$ ,  $V_2$  and all the MFs. The analysis includes the cosmic variance and the statistical error as well as the mask effect. We conclude that the observed lensing MFs are consistent with the standard  $\Lambda$ CDM cosmology.

## 5. SUMMARY AND CONCLUSION

We have used a large number of numerical simulations to examine how masked regions affect the lensing MFs by adopting the actual sky-mask used for a Subaru observation. We have then compared the observed lensing MFs with the results of cosmological simulations to address whether the observed MFs are consistent with the standard cosmological model.

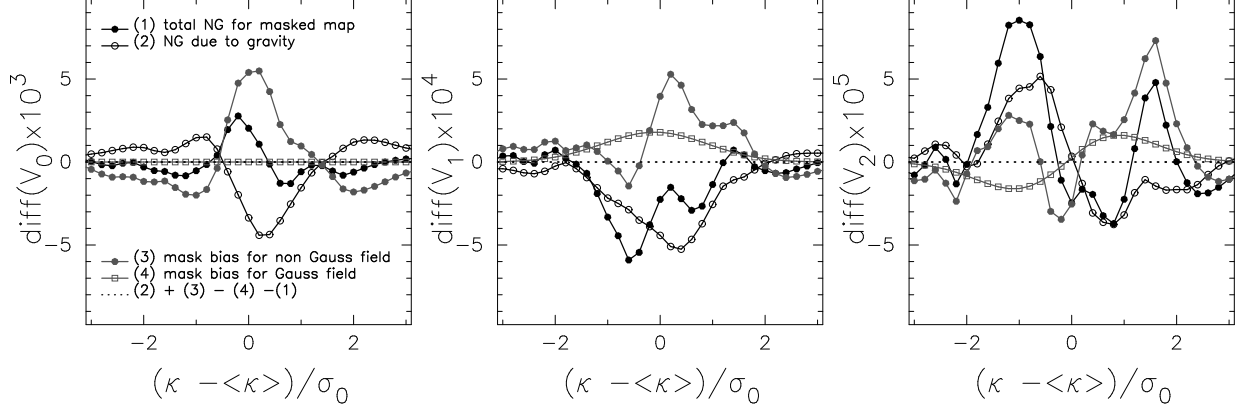


FIG. 3.— We plot the differences between the lensing MFs on masked ray-tracing simulation maps and the Gaussian term. The total non-Gaussianity obtained from the masked maps  $\Delta V_i^{\text{obs}}$  (black line with closed circle), the non-Gaussianity caused by non-linear gravitational growth  $\Delta V_i^{\text{gravity}}$  (black line with open circle), and the bias of lensing MFs due to masked regions for ray-tracing maps  $\Delta V_i^{\text{bias}}$  (gray line with closed circle). We also plot the Gaussian term of  $\Delta V_i^{\text{bias}}$  (gray line with open square). See the definition of each component given by Eq. (16)-(20).

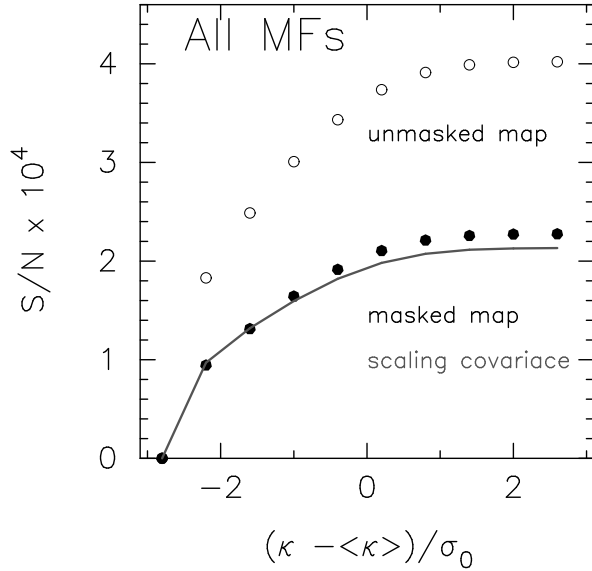


FIG. 4.— The cumulative signal-to-noise ratio for the weak lensing MFs. The horizontal axis represents the maximum value of binned lensing field used in the calculation of  $S/N$ . The open circles are the  $S/N$  for unmasked ‘clean’ lensing maps whereas the black points are for masked maps. The solid line shows  $S/N$  obtained by scaling the covariance matrices of MFs with the effective survey area. We adopt the masked regions used for the Subaru Suprime-Cam data (see Figure 2).

The weak lensing MFs are affected by the lack of cosmic shear data due mostly to foreground contamination. We have used 1000 ray-tracing simulations with masked regions and with realistic shape noises, to show that the non-Gaussianities detected by the MFs do not solely come from gravity induced non-Gaussianities. Masked regions significantly contaminate the *pure* gravitational signals. The bias is induced for the following two reasons: (i) masked regions effectively reduce the number of sampling Fourier modes of cosmic shear and (ii) masked regions introduce variance scatter of the reconstructed weak lensing mass field for each field of view. The former can be corrected analytically at least for a Gaussian random field as shown in the Appendix, while numer-

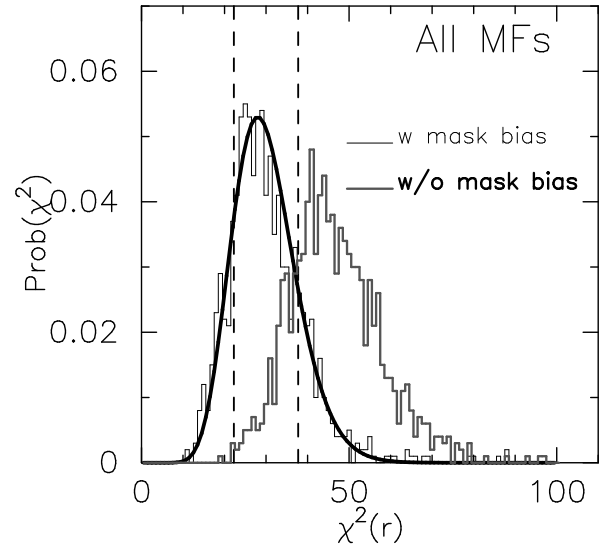


FIG. 5.— We compare the distribution of  $\chi^2(r)$  for  $\mu_i^{\text{theory}}$  evaluated for 1000 masked maps (black histogram) with that for  $\mu_i^{\text{theory}}$  evaluated for 1000 unmasked maps. The thick solid lines is a genuine chi-square distribution with 30 degrees of freedom, and dashed line represents the one sigma region.

ical simulations are needed to include the latter effect accurately.

We then perform a simple analysis to examine the impact of masked regions on the cosmological parameter estimation. From the cumulative signal-to-noise ratio for the lensing MFs, we have found that the cosmological information content in the MFs can be largely determined by the effective survey area. By studying the resulting distribution of the  $\chi^2$  value for simulated maps with masks, we can characterize how the ‘mask bias’ of the MFs affects cosmological constraints. We have shown that most of the resulting  $\chi^2$  values are found outside the expected one sigma region, when the mask is not considered. Clearly the mask bias affect significantly the cosmological parameter estimation.

We have calculated the lensing MFs to the observed weak lensing shear map obtained from a Subaru Suprime-

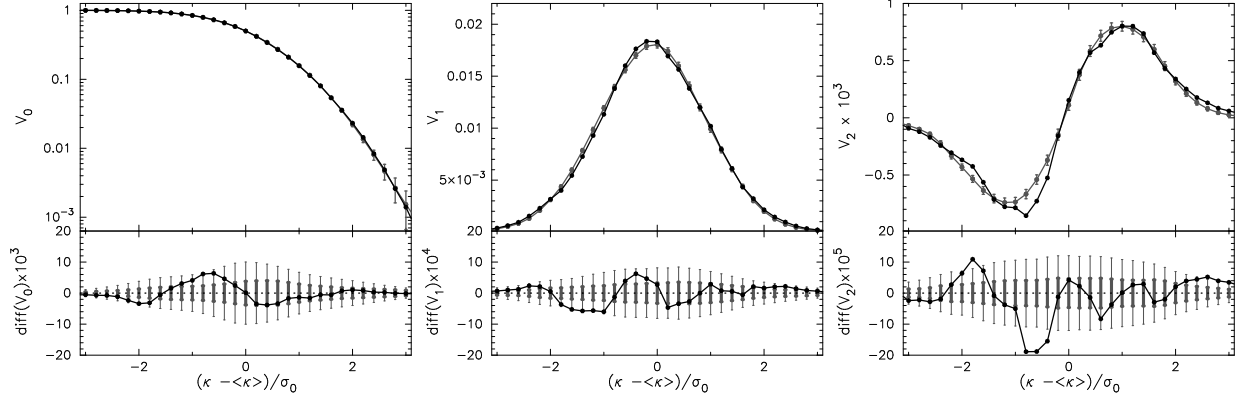


FIG. 6.— We compare the observed MFs with those from cosmological ray-tracing simulations. In the upper panels, the black line shows the observed lensing MFs and the gray one indicates the simulation results. The gray error bars show the cosmic variance obtained from 1000 ray-tracing simulations. In the lower panels, the black line shows the difference between the obtained MFs and the simulation results. The thin error bars are the sum of the cosmic variance and the statistical error while the thick error bars indicate only the cosmic variance. The statistical errors are estimated from 1000 randomized galaxy catalogues.

Cam imaging survey. Our analysis includes, in addition to the cosmic variance, the statistical error estimated from 1000 randomized galaxy catalogs. The resulting  $\chi^2/n_{\text{dof}} = 29.6/30$  for all the MFs suggests that the observed MFs are consistent with the standard adopted  $\Lambda$ CDM cosmology.

Finally, we address the ability of the lensing MFs to constrain cosmological models. By assuming a simple scaling of the covariance matrix of MFs by survey area, we can reduce the error of MFs in each threshold bin by a factor of  $\sim 20$  (100) for upcoming weak lensing surveys with a 1000 (20000)  $\text{deg}^2$  survey area. In the case of a 1000  $\text{deg}^2$  survey, the error in each bin is translated to a  $\sim 5\%$  difference in  $\sigma_8$ . Similarly, for an LSST-like survey with a 20000  $\text{deg}^2$  area, the error in each bin is as small as  $\sim 0.5\%$  in  $\sigma_8$ . The lensing MFs are a promising method for cosmology even with masked regions. It is important to model the effect of mask accurately in order to make the best use of lensing MFs for cosmological constraints. The simplest way would be to use directly the observed mask on ray-tracing simulations as we have done in the present paper. We will need such ray-tracing simulations covering a wide area of more than a thousand square degrees for lensing MFs in upcoming wider surveys.

Further extensive studies are needed in order to devise a way to extract *pure* cosmological information from

the lensing MFs. It is important to study how much systematic non-Gaussianities are introduced by, for example, source galaxy clustering (e.g. Bernardeau 1998), source-lens clustering (e.g. Hamana et al. 2002), the intrinsic alignment (e.g. Hirata & Seljak 2004), and inhomogeneous ellipticity noises due to inhomogeneous surface number density of sources (M. Shirasaki et al., in preparation). The upcoming wide-field surveys will provide highly-resolved lensing maps but with complicated masked regions. Our study in the present paper may be useful to properly analyze the data and to accurately extract cosmological information from them.

We thank Chiaki Hikage and Masahiro Takada for useful discussions. Masanori Sato provided us with their ray-tracing simulations data. M.S. is supported by Research Fellowships of the Japan Society for the Promotion of Science (JSPS) for Young Scientists. This work is supported by World Premier International Research Center Initiative (WPI Initiative), MEXT, Japan and in part by Grant-in-Aid for Scientific Research from the JSPS Promotion of Science (23540324). Numerical computations presented in this paper were in part carried out on the general-purpose PC farm at Center for Computational Astrophysics, CfCA, of National Astronomical Observatory of Japan.

## APPENDIX

### EFFECT OF MASKS ON VARIANCE OF SMOOTHED CONVERGENCE FIELD

Here, we summarize the effect of masked regions on the variance of a smoothed convergence field  $\mathcal{K}$ . When there are masked regions in a survey area, one needs to follow a special procedure in order to construct a smoothed convergence field. Let us define the masked region  $\mathcal{M}_s(\boldsymbol{\theta})$  in a survey area as

$$\mathcal{M}_s(\boldsymbol{\theta}) = \begin{cases} 1 & \text{where } \boldsymbol{\theta} \text{ lies in data region} \\ 0 & \text{otherwise.} \end{cases} \quad (\text{A1})$$

When the area with mask  $\mathcal{M}_s(\boldsymbol{\theta})$  is smoothed, there are ill-defined pixels due to the convolution between  $\mathcal{M}_s$  and a filter function for smoothing  $U(\boldsymbol{\theta})$ . We need to discard the ill-defined pixels to perform statistical analyses. We therefore paste a new mask  $\mathcal{M}_1(\boldsymbol{\theta})$  so that we can mask the ill-defined pixels as well. We then get

$$\mathcal{K}^{\text{obs}}(\boldsymbol{\theta}) = \mathcal{M}_1(\boldsymbol{\theta})\mathcal{K}_1(\boldsymbol{\theta}), \quad (\text{A2})$$

where

$$\mathcal{K}_1(\boldsymbol{\theta}) = \int d^2\phi U(\boldsymbol{\theta} - \boldsymbol{\phi})\mathcal{M}_s(\boldsymbol{\phi})\kappa(\boldsymbol{\phi}). \quad (\text{A3})$$

The variance of the smoothed field is given by

$$\begin{aligned}
\sigma_0^2 &= \frac{1}{S} \int d^2\theta \langle \mathcal{K}^{\text{obs}}(\boldsymbol{\theta})^2 \rangle \\
&= \frac{1}{S} \int d^2\theta \mathcal{M}_1(\boldsymbol{\theta}) \langle \mathcal{K}_1(\boldsymbol{\theta})^2 \rangle \\
&= \frac{1}{S} \int d^2\theta \mathcal{M}_1(\boldsymbol{\theta}) \int \frac{d^2\ell}{(2\pi)^2} \frac{d^2\ell'}{(2\pi)^2} \langle \mathcal{K}_1(\ell) \mathcal{K}_1^*(\ell') \rangle \exp(i(\ell - \ell') \cdot \boldsymbol{\theta}) \\
&= \frac{1}{S} \int \frac{d^2\ell}{(2\pi)^2} \frac{d^2\ell'}{(2\pi)^2} \mathcal{M}_1(\ell - \ell') \langle \mathcal{K}_1(\ell) \mathcal{K}_1^*(\ell') \rangle,
\end{aligned} \tag{A4}$$

where we use the relation  $\mathcal{M}_1(\boldsymbol{\theta})^2 = \mathcal{M}_1(\boldsymbol{\theta})$ . The Fourier mode of  $\mathcal{K}_1$  is given by

$$\begin{aligned}
\mathcal{K}_1(\ell) &= \int d^2\theta d^2\phi U(\boldsymbol{\theta} - \boldsymbol{\phi}) \mathcal{M}_s(\boldsymbol{\phi}) \kappa(\boldsymbol{\phi}) \exp(i\ell \cdot \boldsymbol{\theta}) \\
&= U(\ell) \int \frac{d^2\ell'}{(2\pi)^2} \mathcal{M}_s(\ell') \kappa(\ell - \ell'), \\
\langle \mathcal{K}_1(\ell) \mathcal{K}_1^*(\ell') \rangle &= U(\ell) U^*(\ell') \int \frac{d^2\ell_1}{(2\pi)^2} \frac{d^2\ell'_1}{(2\pi)^2} \mathcal{M}_s(\ell_1) \mathcal{M}_s^*(\ell'_1) \langle \kappa(\ell - \ell_1) \kappa^*(\ell' - \ell'_1) \rangle \\
&= U(\ell) U^*(\ell') \int \frac{d^2\ell_1}{(2\pi)^2} \frac{d^2\ell'_1}{(2\pi)^2} \mathcal{M}_s(\ell_1) \mathcal{M}_s^*(\ell'_1) (2\pi)^2 \delta^{(2)}(\ell - \ell_1 - \ell' + \ell'_1) P_\kappa(|\ell - \ell_1|) \\
&= U(\ell) U^*(\ell') \int \frac{d^2\ell_1}{(2\pi)^2} \mathcal{M}_s(\ell_1) \mathcal{M}_s^*(\ell_1 + \ell' - \ell) P_\kappa(|\ell - \ell_1|)
\end{aligned} \tag{A5}$$

In the following, we assume that  $\mathcal{M}_1(\boldsymbol{\theta})$  is large enough to cover the ill-defined pixels due to smoothing (with a filter function) of the original masked region  $\mathcal{M}_s(\boldsymbol{\theta})$ . This means that, with  $\mathcal{M}_1(\boldsymbol{\theta})$ , there remains only *clean* regions where the smoothed convergence is not affected by the original masked regions  $\mathcal{M}_s(\boldsymbol{\theta})$ . In this case,

$$\mathcal{K}^{\text{obs}}(\boldsymbol{\theta}) \simeq \mathcal{M}_1(\boldsymbol{\theta}) \int d^2\phi U(\boldsymbol{\theta} - \boldsymbol{\phi}) \kappa(\boldsymbol{\phi}). \tag{A6}$$

The fourier mode of  $\mathcal{K}^{\text{obs}}$  can then be given by

$$\begin{aligned}
\mathcal{K}^{\text{obs}}(\ell) &= \int d^2\theta \mathcal{K}^{\text{obs}}(\boldsymbol{\theta}) \exp(i\ell \cdot \boldsymbol{\theta}) \\
&\simeq \int d^2\theta \mathcal{M}_1(\boldsymbol{\theta}) \int d^2\phi U(\boldsymbol{\theta} - \boldsymbol{\phi}) \kappa(\boldsymbol{\phi}) \exp(i\ell \cdot \boldsymbol{\theta}) \\
&= \int d^2\theta' d^2\theta d^2\phi \mathcal{M}_1(\boldsymbol{\theta}') \delta^{(2)}(\boldsymbol{\theta} - \boldsymbol{\theta}') U(\boldsymbol{\theta} - \boldsymbol{\phi}) \kappa(\boldsymbol{\phi}) \exp(i\ell \cdot \boldsymbol{\theta}) \\
&= \int \frac{d^2\ell'}{(2\pi)^2} \int d^2\theta' d^2\theta d^2\phi \mathcal{M}_1(\boldsymbol{\theta}') U(\boldsymbol{\theta} - \boldsymbol{\phi}) \kappa(\boldsymbol{\phi}) \exp(i\ell \cdot \boldsymbol{\theta}) \exp(-i\ell' \cdot (\boldsymbol{\theta} - \boldsymbol{\theta}')) \\
&= \int \frac{d^2\ell'}{(2\pi)^2} \mathcal{M}_1(\ell') \int d^2\theta d^2\phi U(\boldsymbol{\theta} - \boldsymbol{\phi}) \kappa(\boldsymbol{\phi}) \exp(i(\ell - \ell') \cdot \boldsymbol{\theta}) \\
&= \int \frac{d^2\ell'}{(2\pi)^2} \mathcal{M}_1(\ell') U(\ell - \ell') \kappa(\ell - \ell').
\end{aligned} \tag{A7}$$

The variance of the smoothed convergence field is calculated as

$$\begin{aligned}
\sigma_0^2 &= \frac{1}{S} \int d^2\theta \langle \mathcal{K}^{\text{obs}}(\boldsymbol{\theta})^2 \rangle \\
&= \frac{1}{S} \int d^2\theta \int \frac{d^2\ell}{(2\pi)^2} \frac{d^2\ell'}{(2\pi)^2} \langle \mathcal{K}^{\text{obs}}(\ell) \mathcal{K}^{\text{obs}}(\ell') \rangle \exp(-i(\ell - \ell') \cdot \boldsymbol{\theta}) \\
&= \frac{1}{S} \int \frac{d^2\ell}{(2\pi)^2} \langle \mathcal{K}^{\text{obs}}(\ell) (\mathcal{K}^{\text{obs}})^*(\ell) \rangle,
\end{aligned} \tag{A8}$$

where the ensemble average of the Fourier mode is

$$\langle \mathcal{K}^{\text{obs}}(\ell) (\mathcal{K}^{\text{obs}})^*(\ell') \rangle \simeq \int \frac{d^2\ell_1}{(2\pi)^2} \frac{d^2\ell'_1}{(2\pi)^2} \mathcal{M}_1(\ell_1) \mathcal{M}_1^*(\ell'_1) U(\ell - \ell_1) U^*(\ell' - \ell'_1)$$



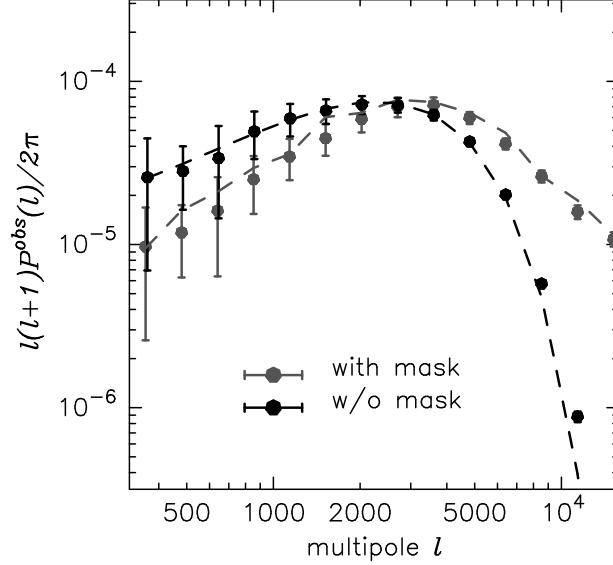


FIG. 7.— We test the validity of Eq.(A6). The gray points with error bars show  $P^{\text{obs}}(\ell)$  obtained from 1000 Gaussian maps with mask  $\mathcal{M}_s(\boldsymbol{\theta})$ . The gray dashed line is the theoretical prediction of Eq.(A11). The black points with error bars show  $P^{\text{obs}}(\ell)$  obtained from 1000 maps without mask. The black dashed line is the input power spectrum smoothed by the Gaussian filter  $U$ .

$$\begin{aligned}
 & \times \langle \kappa(\ell - \ell_1) \kappa^*(\ell' - \ell'_1) \rangle \\
 & = \int \frac{d^2 \ell_1}{(2\pi)^2} \frac{d^2 \ell'_1}{(2\pi)^2} \mathcal{M}_1(\ell_1) \mathcal{M}_1^*(\ell'_1) U(\ell - \ell_1) U^*(\ell' - \ell'_1) \\
 & \quad \times (2\pi)^2 P_\kappa(|\ell - \ell_1|) \delta^{(2)}(\ell - \ell_1 - \ell' + \ell'_1) \\
 & = \int \frac{d^2 \ell_1}{(2\pi)^2} \mathcal{M}_1(\ell_1) \mathcal{M}_1^*(\ell_1 + \ell' - \ell) |U(\ell - \ell_1)|^2 P_\kappa(|\ell - \ell_1|). \quad (\text{A9})
 \end{aligned}$$

We have checked the validity of Eq.(A6) by using 1000 Gaussian simulations. They are the same set of simulations as in Section 2.2. For each Gaussian simulation, we paste the observed masked region  $\mathcal{M}_s(\boldsymbol{\theta})$  from the Subaru Suprime-Cam observation. The map is then smoothed with a Gaussian filter of Eq.(9). The adopted smoothing scale is 1 arcmin. In order to avoid the ill-defined pixels, we paste a new mask  $\mathcal{M}_1(\boldsymbol{\theta})$ , which is constructed conservatively to cover the regions within two times the smoothing scale from the boundary of the original mask  $\mathcal{M}_s(\boldsymbol{\theta})$ . We then calculate

$$P^{\text{obs}}(\ell) \equiv \langle \mathcal{K}^{\text{obs}}(\ell) (\mathcal{K}^{\text{obs}})^*(\ell) \rangle / S. \quad (\text{A10})$$

If  $\mathcal{K}^{\text{obs}}$  can be well-approximated by Eq. (A6), this quantity should be given by

$$P^{\text{obs}}(\ell) \simeq \frac{1}{S} \int \frac{d^2 \ell_1}{(2\pi)^2} |\mathcal{M}_1(\ell_1)|^2 |U(\ell - \ell_1)|^2 P_\kappa(|\ell - \ell_1|). \quad (\text{A11})$$

Figure 7 compares Eq. (A6) and Eq. (A11). Clearly Eq. (A6) is an excellent approximation for the observed survey geometry. The ill-defined pixels are efficiently masked by  $\mathcal{M}_1(\boldsymbol{\theta})$ . We also find the variance  $\sigma_0^2$  decreases by a factor of  $O(5\%)$ . This causes the bias of MFs even if the lensing field is Gaussian.

#### REFERENCES

- Bernardeau, F. 1998, *A&A*, 338, 375  
 Bertin, E. 2006, in *Astronomical Society of the Pacific Conference Series*, Vol. 351, *Astronomical Data Analysis Software and Systems XV*, ed. C. Gabriel, C. Arviset, D. Ponz, & S. Enrique, 112  
 Bertin, E., & Arnouts, S. 1996, *A&AS*, 117, 393  
 Bertin, E., Mellier, Y., Radovich, M., et al. 2002, in *Astronomical Society of the Pacific Conference Series*, Vol. 281, *Astronomical Data Analysis Software and Systems XI*, ed. D. A. Bohlender, D. Durand, & T. H. Handley, 228  
 Bolzonella, M., Miralles, J.-M., & Pelló, R. 2000, *A&A*, 363, 476  
 Erben, T., Van Waerbeke, L., Bertin, E., Mellier, Y., & Schneider, P. 2001, *A&A*, 366, 717  
 Hamana, T., Colombi, S. T., Thion, A., et al. 2002, *MNRAS*, 330, 365  
 Hamana, T., & Mellier, Y. 2001, *MNRAS*, 327, 169  
 Hamana, T., Oguri, M., Shirasaki, M., & Sato, M. 2012, *MNRAS*, 425, 2287  
 Hamana, T., Takada, M., & Yoshida, N. 2004, *MNRAS*, 350, 893  
 Hikage, C., Matsubara, T., Coles, P., et al. 2008, *MNRAS*, 389, 1439  
 Hikage, C., Takada, M., Hamana, T., & Spergel, D. 2011, *MNRAS*, 412, 65  
 Hirata, C., & Seljak, U. 2003, *MNRAS*, 343, 459  
 Hirata, C. M., & Seljak, U. 2004, *Phys. Rev. D*, 70, 063526  
 Hoekstra, H., Franx, M., Kuijken, K., & Squires, G. 1998, *ApJ*, 504, 636

- Huterer, D., Takada, M., Bernstein, G., & Jain, B. 2006, MNRAS, 366, 101
- Kaiser, N. 2000, ApJ, 537, 555
- Kaiser, N., Squires, G., & Broadhurst, T. 1995, ApJ, 449, 460
- Komatsu, E., Smith, K. M., Dunkley, J., et al. 2011, ApJS, 192, 18
- Kratochvil, J. M., Lim, E. A., Wang, S., et al. 2012, Phys. Rev. D, 85, 103513
- Lim, E. A., & Simon, D. 2012, JCAP, 1, 48
- Luppino, G. A., & Kaiser, N. 1997, ApJ, 475, 20
- Matsubara, T., & Jain, B. 2001, ApJ, 552, L89
- Oguri, M., Bayliss, M. B., Dahle, H., et al. 2012, MNRAS, 420, 3213
- Planck Collaboration, Ade, P. A. R., Aghanim, N., et al. 2013, ArXiv e-prints
- Reid, B. A., Percival, W. J., Eisenstein, D. J., et al. 2010, MNRAS, 404, 60
- Sato, J., Takada, M., Jing, Y. P., & Futamase, T. 2001, ApJ, 551, L5
- Sato, M., Hamana, T., Takahashi, R., et al. 2009, ApJ, 701, 945
- Shirasaki, M., Yoshida, N., Hamana, T., & Nishimichi, T. 2012, ApJ, 760, 45
- Smith, R. E., Peacock, J. A., Jenkins, A., et al. 2003, MNRAS, 341, 1311
- Spergel, D. N., Bean, R., Doré, O., et al. 2007, ApJS, 170, 377
- Tegmark, M., Eisenstein, D. J., Strauss, M. A., et al. 2006, Phys. Rev. D, 74, 123507
- Tomita, H. 1986, Progress of Theoretical Physics, 76, 952
- Wang, S., Haiman, Z., & May, M. 2009, ApJ, 691, 547
- Weinberg, D. H., Gott, III, J. R., & Melott, A. L. 1987, ApJ, 321, 2
- White, M., & Hu, W. 2000, ApJ, 537, 1
- Winitzki, S., & Kosowsky, A. 1998, NewA, 3, 75